Retrieval of Polar Stratospheric Cloud Microphysical Properties From Lidar Measurements: Dependence on Particle Shape Assumptions

J. Reichardt[1,2], S. Reichardt[1,2], P. Yang[3,4], T. J. McGee[2]

1. Joint Center for Earth Systems Technology, University of Maryland Baltimore County, Baltimore, MD
2. Atmospheric Chemistry and Dynamics Branch, Laboratory for Atmospheres, NASA Goddard Space Flight Center, Greenbelt, MD
3. Goddard Earth Sciences and Technology Center, University of Maryland Baltimore County, Baltimore, MD
4. Climate and Radiation Branch, Laboratory for Atmospheres, NASA Goddard Space Flight Center, Greenbelt, MD

Submitted to

Journal of Geophysical Research

Corresponding author address: Dr. Jens Reichardt, Code 916, NASA Goddard Space Flight Center, Greenbelt, MD 20771; Phone: 301-614-5989; Fax: 301-614-5903; Email: reichardt@code916.gsfc.nasa.gov.

Abstract

A retrieval algorithm has been developed for the microphysical analysis of polar stratospheric cloud (PSC) optical data obtained using lidar instrumentation. The parameterization scheme of the PSC microphysical properties allows for coexistence of up to three different particle types with size-dependent shapes. The finite difference time domain (FDTD) method has been used to calculate optical properties of particles with maximum dimensions $\leq 2\,\mu$m and with shapes that can be considered more representative of PSCs on the scale of individual crystals than the commonly assumed spheroids. Specifically, these are irregular and hexagonal crystals. Selection of the optical parameters that are input to the inversion algorithm is based on a potential data set such as that gathered by two of the lidars on board the NASA DC-8 during the Stratospheric Aerosol and Gas Experiment (SAGE) Ozone Loss Validation Experiment (SOLVE) campaign in winter 1999/2000: the Airborne Raman Ozone and Temperature Lidar (AROTEL) and the NASA Langley Differential Absorption Lidar (DIAL). The microphysical retrieval algorithm has been applied to study how particle shape assumptions affect the inversion of lidar data measured in leewave PSCs. The model simulations show that under the assumption of spheroidal particle shapes, PSC surface and volume density are systematically smaller

than the FDTD-based values by, respectively, $\sim$ 10–30% and $\sim$ 5–25%.

Index terms: 0300, 0305, 0320, 0360, 0394.

1. Introduction

Recent studies raise concerns about a positive feedback between the anthropogenically induced climate change and stratospheric ozone depletion [*Hartmann et al.*, 2000]. It is predicted that increasing concentrations of atmospheric carbon dioxide will affect the stratosphere in two ways: First, stratospheric temperatures will decrease [*Shindell et al.*, 1998], and second, the input of water vapor into the stratosphere will increase due to higher temperatures at the tropical tropopause [*Kirk-Davidoff et al.*, 1999]. These effects will result in polar vortices that are more stable, in expanded regions of polar stratospheric cloud (PSC) formation, and in an increase in the number and extent of PSCs [*Butchart et al.*, 2000]. The cumulative effect of these changes will be an increase in ozone depletion. In turn, the reduction of stratospheric ozone concentrations will influence tropospheric greenhouse warming via dynamical, chemical, and radiative feedbacks [*Hartmann et al.*, 2000].

In this context knowledge of particle sizes and number densities of PSCs is highly important, because they are critical parameters for the modeling of stratospheric chemical processes that lead to the destruction of ozone: Conversion rates of inert reservoir gases into potentially ozone-destroying chemical compounds strongly depend on the phase of the PSC particles and the particle surface area available for heterogeneous processing [*Ravishankara and Hanson*, 1996]. The size of the PSC particles determines the

sedimentation velocity and hence the denitrification and dehydration of the stratosphere.

One approach to derivation of microphysical parameters of stratospheric particles is interpretation of optical data measured *in situ* with optical particle counters (OPC), or remotely with lidar. Inversion of optical data from PSCs that consist of liquid ternary aerosols (LTA, aqueous solutions of nitric and sulfuric acid) [*Mehrtens et al.*, 1999] or from stratospheric background aerosol [*Jäger and Hofmann*, 1991; *Deshler et al.*, 1992; *Wandinger et al.*, 1995; *Borrmann et al.*, 2000b] can be accomplished, because the particles are spherical and Mie theory applies.

For PSCs that are formed from solid particles [water ice and nitric acid hydrates (NAH)] *in situ* particle sampling, though rare, revealed PSC crystals of irregular, hexagonal, or trigonal shape [*Goodman et al.*, 1989]. For these particles a suitable scattering theory has not been readily available up to now. As a consequence, the T-matrix method [*Mishchenko*, 1991] for calculation of optical properties of spheroids is used for the microphysical lidar data analysis, because it permits interpretation of the depolarization produced by these PSC types [*Carslaw et al.*, 1998; *Wirth et al.*, 1999; *Tsias et al.*, 1999; *Reichardt et al.*, 2000; *SOLVE · Theseo 2000 Science Meeting*, 2000]. However, as pointed out by *Reichardt et al.* [2000], this T-matrix approach relies on the assumption that the optical properties of an ensemble of spheroids resemble those of crystalline PSCs with similar particle size

distributions and particle number densities. While the effects of particle nonsphericity on OPC measurements of particle microphysical properties have been evaluated [*Whitby and Vomela*, 1967; *Baumgardner et al.*, 1992; *Dye et al.*, 1992; *Borrmann et al.*, 2000a], a detailed error treatment of lidar data inversion that is based on the T-matrix method has not been carried out so far.

Recently, the finite-difference time-domain (FDTD) technique has become available for calculation of optical properties of small particles of arbitrary shape with high accuracy (normally $< 1\%$) [*Yang and Liou*, 1996; *Yang and Liou*, 1998; *Yang et al.*, 2000]. The volume of the scattering particle is discretized by using a Cartesian grid mesh which allows construction of particles with corners, edges, and flat crystal faces that can be regarded as representative of crystalline PSCs. This paper focuses on the dependence of the retrieval of PSC microphysical properties from lidar measurements on particle shape assumptions. The approach can be described as follows. Based on Mie and FDTD calculations we generate lidar-relevant optical properties of PSCs, assuming realistic mixtures of droplets, irregular and hexagonal crystals. Selection of optical parameters is based on the measurements acquired by two of the lidars which were operated on the NASA DC-8 during the Stratospheric Aerosol and Gas Experiment (SAGE) Ozone Loss Validation Experiment (SOLVE) campaign in winter 1999/2000 [*McGee et al.*, 2000; *Hostetler et al.*, 2000; *Butler et al.*, 2001]. Then we apply a

T-matrix based retrieval algorithm to the simulated data to extract microphysical information, and finally we compare initial and retrieved PSC microphysical properties. FDTD calculations are computer intensive, with calculation time roughly proportional to the volume of the scattering particle. E.g., determination of the scattering phase matrix at 355 nm for a NAT PSC particle with a maximum dimension of 2 μm and an aspect ratio of 0.5 requires two weeks of computation time on a SGI octane2 workstation (360 MHz). Therefore the maximum size of the particles that can be considered in this study is 2 μm, and for this reason this study is restricted to the analysis of PSCs composed of small solid particles. In particular, this investigation is most applicable to leewave-induced PSCs [*Tabazadeh et al.*, 1997; *Carslaw et al.*, 1998; *Tsias et al.*, 1999]. In Section 2 the relation between particle microphysical properties and optical parameters that can be measured with lidars is reviewed. Next we describe the microphysical retrieval algorithm that is used for inversion of lidar data (Section 3). In Section 4 the results of FDTD computations for single crystals are presented, followed by an intercomparison between the FDTD- and T-matrix-based techniques in Section 5. A summary of this study is given in Section 6.

2. Microphysical and Optical PSC Properties

The optical and microphysical parameters of a cloud are related indirectly. The optical properties at a certain cloud height are averages over all light scattering processes by individual cloud particles at this height (single

scattering is assumed). Particle scattering is determined by the scattering phase matrix which in turn depends on the size, shape and composition of the particles. If latter are to be retrieved from lidar measurements, further difficulties stem from the observation geometry. Lidars exclusively sense the backscattering direction of clouds, so that only the information content of the scattering matrices at 180° scattering angle can be exploited. Inversion of lidar measurements of crystalline PSCs is therefore an ill-posed problem which makes derivation of microphysical properties a challenging task.

As previously mentioned, PSC volume density V, surface density A, and particle size spectrum are of special interest. V is given by

$$V = N \int_d [v(\delta)\hat{n}(\delta)]\,\mathrm{d}\delta. \tag{1}$$

A is described by a similar equation. In Eq. (1), N is the number density of the cloud particles, v is the particle volume, and $\hat{n}$ is the normalized size distribution ($\int_d \hat{n}(\delta)\,\mathrm{d}\delta = 1$). We choose to parameterize $\hat{n}$ and v in terms of the maximum dimension d of the particles, in a manner similar to that used in the cirrus cloud studies of *Auer and Veal* [1970] and *Heymsfield and Platt* [1984].

The complexity of lidar systems used for PSC observations determines the number of PSC optical parameters that can be measured. In the following we give a summary of the optical quantities that are accessible to lidar remote sensing in principle. The first two parameters, the particle extinction

coefficient α_{par} and the backscatter coefficient β_{par}, depend on the particle number density of the PSC. The extinction coefficient is given by

$$\alpha_{par}(\lambda) = N \int_d [Q^{sca}(\lambda, \delta) G(\delta) \hat{n}(\delta)] d\delta, \quad (2)$$

where Q^{sca} is the scattering efficiency of the PSC particle, and G is its geometrical scattering cross section. In addition to the explicit dependences on wavelength and maximum dimension shown in Eq. (2), Q^{sca} also depends on the index of refraction of the scattering particles, and both Q^{sca} and G are functions of the particles' morphology. In this study we assume that the PSC particles do not absorb light at the laser wavelengths.

The backscatter coefficient is defined by

$$\beta_{par}(\lambda) = N \int_d [p^{\pi}(\lambda, \delta) Q^{sca}(\lambda, \delta) G(\delta) \hat{n}(\delta)] d\delta. \quad (3)$$

p^{π} denotes the value of the scattering phase function p at the backscattering direction. For PSCs it can be assumed that the cloud particles are randomly oriented ($p = p(\vartheta)$, where ϑ is the scattering angle). The scattering phase function shown in this paper satisfy the normalization condition

$$2\pi \int_0^{\pi} [p(\vartheta) \sin \vartheta] d\vartheta = 1. \quad (4)$$

so that p can be interpreted as the probability distribution function of the scattered energy. PSC extinction and backscatter coefficients can be measured with Raman lidars [*Ansmann et al.*, 1992]. Because of their

dependence on N, α_{par} and β_{par}, and likewise the backscatter ratio (ratio of total to molecular backscattering), cannot be used directly for determination of the particle properties. Preferably, lidar optical properties should be used, if available, which do not depend on the particle number density, and which therefore contain information about the scattering properties of the cloud particles alone. Specifically, these are lidar ratio

$$S_{\mathrm{par}}(\lambda) = \alpha_{\mathrm{par}}(\lambda)/\beta_{\mathrm{par}}(\lambda), \tag{5}$$

color ratio

$$C_{\mathrm{par}}(\lambda_k, \lambda_l) = \beta_{\mathrm{par}}(\lambda_k)/\beta_{\mathrm{par}}(\lambda_l), \quad l = k+1, k = 1 \ldots k_{\max} - 1, \tag{6}$$

and depolarization ratio

$$\Delta_{\mathrm{par}}(\lambda) = \beta^{\perp}_{\mathrm{par}}(\lambda)/\beta^{\parallel}_{\mathrm{par}}(\lambda), \tag{7}$$

where $\beta^{\perp}$ and $\beta^{\parallel}$ are the backscatter coefficients in the polarization planes orthogonal and parallel, respectively, to the linearly polarized lidar radiation source:

$$\beta^{\perp}_{\mathrm{par}}(\lambda) = N \int_d [\frac{\Delta(\lambda, \delta)}{1 + \Delta(\lambda, \delta)} p^{\pi}(\lambda, \delta) Q^{\mathrm{sca}}(\lambda, \delta) G(\delta) \hat{n}(\delta)] \mathrm{d}\delta, \tag{8}$$

$$\beta^{\parallel}_{\mathrm{par}}(\lambda) = N \int_d [\frac{1}{1 + \Delta(\lambda, \delta)} p^{\pi}(\lambda, \delta) Q^{\mathrm{sca}}(\lambda, \delta) G(\delta) \hat{n}(\delta)] \mathrm{d}\delta. \tag{9}$$

Here Δ denotes the depolarization ratio of particles with maximum dimension d. For measurements of color ratios multiwavelength lidars with at

least two transmitted wavelengths ($k_{max} = 2$) are required, Δ_{par} can be measured with polarization lidars.

3. Retrieval Algorithm

Computations of scattering phase matrices can be carried out for a limited number of particle sizes and shapes only. Consequently, for calculation of PSC optical properties the defining equations for the extinction and backscatter coefficients [Eqs. (2), (3), (8), and (9)] have to be partially discretized. Formally, the approach used here can be described for all coefficients by

$$X(\lambda) = N \sum_i \left\{ Y(\lambda, d_i) \int_{\max[d_{min}, d_{min}(i)]}^{\min[d_{max}, d_{max}(i)]} [Q^{sca}(\lambda, \delta) G(\delta) \hat{n}(\delta)] d\delta \right\}, \qquad (10)$$

if the functions given in Table 1 are substituted for X and Y. For this study, scattering phase matrices have been calculated for 17 particles ($i = 17$) with maximum dimensions d_i between 0.2 and 2.0 μm. Table 2 summarizes d_i and the lower and upper boundaries of the range of application of Y, $d_{min}(i)$ and $d_{max}(i)$. Q^{sca} and G, which are also determined with the optical-property calculations, usually exhibit a smooth dependence on d. So instead of summing over the discrete values of Q^{sca} and G we use interpolated Q^{sca} data and polynomial fits to G for the computation of the integral in Eq. (10). In Eq. (10), d_{min} and d_{max} are the lower and upper boundaries of $\hat{n}$.

If different types of particles are assumed to coexist in the PSC, Eq. (10) has

to be rewritten as

$$X(\lambda) = N \sum_j \sum_i \left\{ Y_j(\lambda, d_i) \int_{\max[d_{\min}, d_{\min}(i)]}^{\min[d_{\max}, d_{\max}(i)]} [f_j(\delta) Q_j^{\mathrm{sca}}(\lambda, \delta) G_j(\delta) \hat{n}(\delta)] \mathrm{d}\delta \right\}, \tag{11}$$

with

$$\sum_j f_j(d) = 1 \tag{12}$$

for all d.

For our investigations we assume that five PSC particle properties, specifically $S_{\mathrm{par}}(532\,\mathrm{nm})$, $C_{\mathrm{par}}(355\,\mathrm{nm}, 532\,\mathrm{nm})$, $C_{\mathrm{par}}(532\,\mathrm{nm}, 1064\,\mathrm{nm})$, $\Delta_{\mathrm{par}}(532\,\mathrm{nm})$, and $\Delta_{\mathrm{par}}(1064\,\mathrm{nm})$, are available. This data set was measured with, e.g., two of the lidars on board the NASA-DC8 during the SOLVE mission in winter 1999/2000. These were the four-wavelength Airborne Raman Ozone and Temperature Lidar AROTEL [*McGee et al.*, 2000] that was complemented by a polarization-sensitive aerosol detection receiver [*Hostetler et al.*, 2000], and the DIAL system [*Butler et al.*, 2001]. The five particle optical properties allow for optimization of an equal number of microphysical parameters with the retrieval algorithm. To assess the performance of T-matrix-based retrieval techniques, we model the optical properties of a PSC with given microphysical parameter set by use of FDTD and Mie data. Then the simulated lidar data is analyzed assuming spheroidal particle shapes. In what follows, descriptions of the microphysical model assumptions and of the parameterization are given.

3.1. Model assumptions

Our model assumptions are based on the following scenario of formation of solid PSC particles. Wind flow over orographic features may, under certain conditions [*Dörnbrack et al.*, 2001], result in wave activity downwind, and in localized temperature minima in the stratosphere. Stratospheric liquid aerosols carried through these cold regions with the wind are cooled rapidly. At temperatures $T <\sim 195\,\mathrm{K}$ the aerosols grow by uptake of H_2O and HNO_3 to form LTA [*Carslaw et al.*, 1994]. If the air parcel cools to temperatures 3–4 K below the ice equilibrium temperature T_{ice}, water ice embryos form heterogeneously within the LTA droplets [*Tabazadeh et al.*, 1997; *Carslaw et al.*, 1998]. NAH particles also nucleate in leewave PSCs, probably heterogeneously on the ice particles (ice-mediated NAH formation) [*Koop et al.*, 1997; *Carslaw et al.*, 1999]. Depending on T, the solid particles grow or evaporate by mass transfer from or to the vapor phase. For $T < T_{\mathrm{ice}}$, ice, NAH and LTA coexist. In the Arctic, this will only be the case in the coldest regions of a leewave temperature perturbation. On temperature increases to $T > T_{\mathrm{ice}}$ further downwind, the ice particles evaporate. However, under favorable synoptic conditions NAH particles survive and can be detected several hundreds of kilometers away from their origin [*Carslaw et al.*, 1998; *Tsias et al.*, 1999; *Voigt et al.*, 2000].

3.1.1 Size of the PSC particles

In situ data suggest a power-law dependence of the number density on

particle diameter for PSCs that contain solid particles [*Dye et al.*, 1992]. For this reason we choose for the normalized size spectrum $\hat{n}$:

$$\hat{n} = \frac{c+1}{d_{\max}^{c+1} - d_{\min}^{c+1}} d^c. \tag{13}$$

Slope c and the upper boundary $d_{\max}$ of the spectrum are optimized during the retrieval process.

The number density of the solid PSC particles is determined by the nucleation processes. The fraction of the LTA droplets that nucleate ice depends on the cooling rate in the leewave [*Tabazadeh et al.*, 1997]. The fraction of ice particles that serve as NAH nuleation sites depends on the atmospheric conditions and may vary considerably [*Carslaw et al.*, 1998; *Wirth et al.*, 1999]. Calculations by *Tabazadeh et al.* [1997] and *Carslaw et al.* [1998] show that high cooling rates will result in large number densities of small solid particles $<\sim 2\,\mu$m, and *in situ* observations support the theoretical values [*Voigt et al.*, 2000]. In our retrieval algorithm we vary $d_{\max}$ accordingly to values up to $2\,\mu$m. The lower boundary of the assumed particle distribution is fixed at $d_{\min} = 0.175\,\mu$m. This approach is not problematic, because scattering of very small particles does not contribute significantly to the lidar signals.

3.1.2. Shape of the PSC particles

We assume three principal particle shapes: spheres, irregular and hexagonal crystals. *Pueschel et al.* [1992] show photos of irregular submicron solid

particles formed in evaporating LTA droplets that impacted the Formvar coating of glass strips. These photos illustrate nicely how PSC particles might look like that nucleated homogeneously in stratospheric LTA. *In situ* measurements in contrails also demonstrate that the smallest particles are irregular ice crystals [*Goodman et al.* 1998]. Contrarily, larger ice crystals exhibit well-defined symmetries. 5-50 μm ice crystals sampled in the Antarctic stratosphere [*Goodman et al.*, 1989] and in a cirrus cloud that formed under conditions similar to those of PSC formation [*Heymsfield*, 1986] were predominantly hexagonal columns and trigonal plates. In the case of contrails, hexagonal plates have been found to be the prevalent shape [*Goodman et al.* 1998].

For this reason hexagonal crystals in our model represent PSC particles that acquired crystal symmetry by growing to a certain size. Irregular crystals are thought to be representative of newly formed ice embryos, which are generally smaller than the hexagonal crystals. We assume the same particle shapes for water ice and NAH; LTA droplets are accounted for by spheres. Size-dependent fractions f_j of the three particle types are parameterized as

$$f_1(d) = \frac{1}{2}\{1 + \tanh[3\,\mu\mathrm{m}^{-1}(d - d_{0.5})]\} \quad \text{(hexagonal crystals)}. \tag{14}$$

$$f_2(d) = [1 - f_1(d)]\{1 - \exp[-(d - 0.1\,\mu\mathrm{m})^2/\sigma^2]\} \text{ (irregular crystals)}, \tag{15}$$

$$f_3(d) = [1 - f_1(d)]\exp[-(d - 0.1\,\mu\mathrm{m})^2/\sigma^2] \quad \text{(spheres)}. \tag{16}$$

f_j are determined by the two parameters $d_{0.5}$ and σ which are variables of the

optimization algorithm. This parameterization allows for PSCs that are formed of any of the three particle types alone, and for mixtures of two or three particle shapes.

Aspect ratio a (ratio of the length of the particle along the symmetry axis to particle widths; columns and prolate spheroids have $a > 1$, plates and oblate particles have $a < 1$) of the crystalline PSC particles is assumed to be size dependent as well. Measurements in stratospheric and tropospheric ice clouds confirm that a increases with particle size. Very small ice particles have aspect ratios close to one. We apply these results to the PSC particles by assuming

$$a(d) = 1 + m(d - 0.175\,\mu\text{m}), \quad d \le d', \tag{17}$$

with $a(d') = 1.5$ (prolate particles) or $a(d') = 0.5$ (oblate particles). For $d > d'$ we set $a(d) = a(d')$. Slope m is optimized in the retrieval. For the model comparison presented here optical data for aspect ratios of 0.5, 0.75, 1.0, 1.25, and 1.5 have been available. Figure 1 illustrates the size dependences of $\hat{n}$, f_1–f_3, and a. For this particular example $d_{\max}$, c, $d_{0.5}$, σ, and m are 1.8 μm, −4, 1.0 μm, 0.25 μm, and 0.4 μm^{-1}, respectively.

3.1.3. Refractive index of the PSC particles

Light absorption by PSC particles is not considered. The refractive indices of LTA at the three laser wavelengths are taken from *Luo et al.* [1996] ($T = 191$ K). Refractive indices of the irregular particles and the hexagonal

crystals can be chosen independently. For water ice, refractive indices of *Warren* [1984] are used which have been confirmed in ice PSCs [*Adriani et al.*, 1995]. The refractive index of NAH is a function of the H_2O:HNO_3 molar ratio [*Middlebrook et al.*, 1994]. If initially water-rich NAH particles rather than NAT nucleated on the ice embryos in the LTA droplets, these particles would have refractive indices smaller than NAT. Over time NAH composition and refractive index would then slowly change to the values of the thermodynamically favored NAT [*Marti and Mauersberger*, 1993]. *In situ* data generally confirm the existence of NAT particles in the stratosphere [*Fahey et al.*, 1989; *Kawa et al.*, 1992; *Voigt et al.*, 2000], although exceptions were found [*Kawa et al.*, 1992]. Here we assume that the nitric acid particles are NAT. As refractive indices we take the values measured by *Deshler et al.* [2000] in a depolarizing Arctic PSC of type I (presumably NAT), although these values are higher than those found in Antarctic PSCs by the same method [*Adriani et al.*, 1995] and seem to be more in agreement with NAH of smaller water content than NAT [*Middlebrook et al.*, 1994]. The data of *Deshler et al.* [2000] might therefore be regarded as an upper limit to the refractive indices of NAH PSCs.

3.2. Computation of single-crystal phase matrices

Phase matrices of hexagonal and irregular crystals were calculated with the FDTD code described by *Yang and Liou* [1996], *Yang and Liou* [1998] and *Yang et al.* [2000]. Irregular particles are crystals with seven corners and ten

flat crystal faces. Details about the realization of these particles are given by *Yang et al.* [2000]. Calculations for spheroids with $a \neq 1$ were carried out with a T-matrix code which is available at http://www.giss.nasa.gov/~crmim/t_matrix.html [*Mishchenko*, 1991]. For the computation of phase functions of spheres we used the Mie code of *van de Hulst* [1981]. We smoothed out the Mie resonances of $p(d_i)$ by using a projection area weighted normal size distribution with center d_i and an effective variance [Hansen and Travis, 1974] of 0.0067 for the calculations. The integration interval then roughly corresponds with the application ranges of d_i for all discrete particle sizes. For the sake of conciseness, the same approach was followed for spheroids with $a \neq 1$.

4. FDTD Calculations of Single Crystals

In Fig. 2 phase functions of particles with different shapes are compared. The shapes of the phase functions for given d and a are similar, yet differences in the backscattering direction exist that are important for lidar observations. At 180° scattering angle hexagonal plates scatter more and hexagonal columns less than the corresponding spheroids. As in both cases the projection areas G of the hexagons are larger than those of the spheroids, this behavior cannot be explained by differences in G, but must be an effect of the particle shape. Similarly, irregular crystals with $d = 1.6\,\mu$m backscatter less than spheroids with $d = 1.0\,\mu$m, although G values are comparable. From this we conclude that substituting spheroids with equal G for crystals

does not reproduce the optical properties on the scale of individual crystals. This has to be kept in mind when retrieval of microphysical parameters from lidar data is attempted with a T-matrix-based inversion scheme and a parameterization of PSC particle size distributions in terms of surface equivalent radius.

The size dependence of the lidar-relevant optical properties of single PSC particles is illustrated in Fig. 3. Q^{sca} exhibits oscillatory patterns which depend on the volume and the refractive index of the PSC particles. For particle sizes with Q^{sca} values on the rising slope of the first Q^{sca} maximum, lidar ratios are largest. For aspect ratios of 0.5 and 1.5, Q^{sca} of NAT hexagons with $d >\sim 1.4\,\mu$m is close to the geometrical-optics limiting value of two. These particles have lidar ratios that are relatively independent of d and that are in the range of values found in cirrus clouds where scattering by particles $> 10\,\mu$m is dominant. This suggests that the geometrical-optics approximation might be applicable to calculation of the optical properties of NAT hexagons with aspect ratios near one and dimensions $> 2\,\mu$m. Because FDTD computations for this type of particles are especially time consuming, this result is important for future extension of our PSC particle data base to larger sizes. Depolarization ratios shown in Fig. 3 generally increase with particle maximum dimension.

In Fig. 4 the dependences of the PSC particle optical properties on aspect ratio are presented. For all particle sizes, Q^{sca}, S, and Δ vary smoothly with

a. This behavior has been exploited for the FDTD-based retrieval algorithm where optical properties of particles with aspect ratios other than those listed in Section 3.1.2 are derived by interpolation. For $d = 0.4\,\mu$m depolarization ratio increases monotonously with a. In the case of the larger particles, Δ values are minimum for thick to equidimensional plates. Generally, light scattering by columns leads to higher Δ than scattering by plates.

The wavelength dependence of Q^{sca}, S, and Δ is highlighted in Fig. 5. Computational results obtained for a hexagonal NAT plate ($a = 0.5$) are shown. For all wavelengths low S correspond with high Δ values, and vice versa. At 1064 nm, plates $< 1.2\,\mu$m do not depolarize, whereas at shorter wavelengths high Δ values are found. This high sensitivity of Δ to particle size and wavelength suggests to include lidar measurements of depolarization ratio at 1064 nm, and at 532 or 355 nm in the microphysical retrieval.

5. Retrieval Intercomparison

The parameter sets used for calculation of the initial optical properties $S_{\text{par}}(532\,\text{nm})$, $C_{\text{par}}(355\,\text{nm}, 532\,\text{nm})$, $C_{\text{par}}(532\,\text{nm}, 1064\,\text{nm})$, $\Delta_{\text{par}}(532\,\text{nm})$, and $\Delta_{\text{par}}(1064\,\text{nm})$ are summarized in Tab. 3. The initial model data is input to the T-matrix-based retrieval program. Here, the microphysical parameters are iteratively chosen within reasonable limits, and the PSC optical properties calculated. The accuracy of these data is determined with a χ^2 test. Statistical weights reflect measurement uncertainties, e.g., lidar ratio

has a smaller statistical weight than color ratio or depolarization ratio. Since we assume both irregular and hexagonal particles to be composed of NAT, parameter $d_{0.5}$ is only relevant for the initial FDTD computations. It is meaningless for the retrieval, and is therefore held constant at 1.0 μm during optimization.

In Plate 1 initial microphysical parameters and best fits are summarized for model runs with different size distributions, but same σ, m, and $d_{0.5}$. Generally, the retrieved values of the asphericities of the spheroids and $d_{\max}$ of the size distribution are larger than the initial values. This is probably an effect of the high statistical weight of the depolarization data: In contrast to equidimensional crystals, spheroids with $a = 1$ do not depolarize light at 180° scattering angle. In order to match the FDTD depolarization ratios of equidimensional to columnar crystals ($m = 0.4\,\mu\text{m}^{-1}$), the asphericities of the spheroids have to be maximized, hence the large deviations between initial and retrieved m. Aspherical particles, however, have smaller volumes than compact particles of the same maximum dimension, and this is compensated for by preferably increasing $d_{\max}$ and slightly adjusting slope c of the size distribution. The width of the LTA mode (σ) is well retrieved in all cases.

The effects of solid-particle asphericity are studied with model runs 7–9 (Plate 2). If plate-like crystals are assumed (parameter set 7), the size distribution is recovered. However, highest accuracy is found for prolate spheroids with large aspect ratios even for small d ($m > 1.0\,\mu\text{m}^{-1}$). In runs 8

and 9, agreement between retrieved and initial parameters is poor. E.g., in model run 8, optical properties of PSCs with few small droplets ($\sigma = 0.1\,\mu$m) and equidimensional crystals that slowly develop into elongated particles ($m = 0.4\,\mu\text{m}^{-1}$) are fitted with particle ensembles that predominantly consist of droplets and highly aspherical spheroids below and above $d = 1.0\,\mu$m, respectively. The effect of the large droplets on Δ_{par} is compensated for by increased scattering contributions of large spheroids (high d_{max} and c values). Although initial parameter sets 5 and 8 only differ in σ, the retrieved parameters show large differences. This is because lidar data are ambiguous: For a given set of optical PSC properties no unique solution to the inversion problem exists, and consequently any generic inversion algorithm is unstable. This problem has to be addressed by introducing additional retrieval constraints based on microphysical considerations. *Carslaw et al.* [1998], e.g., checked microphysical and optical modeling results for consistency in order to interpret PSC lidar data by use of the T-matrix method. Parameter sets 10 and 11 represent PSCs with LTA droplets being the dominant particles $< 1\,\mu$m, and parameter set 12 describes the extreme case of a PSC that is almost exclusively formed from columnar hexagons (Plate 2). In all cases $\hat{n}$ is retrieved well, yet m and σ do not match the initial values.

So far we have studied how the individual parameters of our model parameterization depend on the assumed principal particle shapes. Now we examine the effect the shape assumptions have on PSC bulk properties that

are important for stratospheric chemical and microphysical modeling. specifically PSC particle surface area density A and volume density V. In Plate 3 relative differences δA between retrieved and initial surface density $[\delta A = (A_r - A_i)/A_i]$ are plotted against corresponding relative differences δV. In all cases retrieved A and V are smaller than the initial values (δA and $\delta V < 0$). The only exception is model run 12 for the PSC that consists of hexagonal crystals only, a case that can be regarded as unrealistic. Generally, absolute values of δV are smaller than those of δA. The important conclusion is that, if scattering by solid PSC particles is assumed to be better represented by phase matrices of irregular and hexagonal crystals than by those of spheroids, T-matrix-based microphysical retrieval algorithms tend to systematically underestimate PSC surface and volume density. In our model simulations of leewave PSCs formed from LTA and NAT particles, the retrieved values for A and V are found to be, respectively, $\sim$ 10–30% and $\sim$ 5–25% smaller than the initial values, in some cases deviations are even larger. These shape-assumption related uncertainties have to be accounted for in PSC modeling efforts that are based on lidar measurements.

6. Summary

An algorithm has been developed for retrieval of microphysical properties from PSC lidar data. The parameterization scheme allows for coexistence of up to three different particle types with size-dependent shapes. The optical properties of solid particles $< 2\,\mu$m have been determined with the FDTD

technique, the particles have irregular or hexagonal shape. In this work, the FDTD-based algorithm has been applied to investigate the effect of particle shape assumptions on the inversion of lidar data measured in leewave PSCs. The simulations show that the assumption of spheroidal PSC particles results in the retrieval of larger maximum particle sizes and higher asphericities when compared to model runs with irregular and hexagonal particles. Furthermore, leewave PSC surface and volume density are systematically smaller by, respectively, $\sim$ 10–30% and $\sim$ 5–25%.

We plan to extend our FDTD data base to larger particles, and to include particles with other geometries and refractive indices. Furthermore we will incorporate geometrical-optics computations of optical properties of particles to which this approximation applies in our microphysical analysis of PSCs.

Acknowledgments. We would like to thank P. A. Newman and J. F. Gleason for computational support. This work was funded in part by a grant from NASA's Atmospheric Chemistry Modeling and Analysis Program.

References

Adriani, A., T. Deshler, G. Di Donfrancesco, and G. P. Gobbi, Polar stratospheric clouds and volcanic aerosol during spring 1992 over McMurdo Station, Antarctica: Lidar and particle counter comparisons, *J. Geophys. Res.*, *100*, 25,877–25,897, 1995.

Ansmann, A., U. Wandinger, M. Riebesell, C. Weitkamp, and W. Michaelis, Independent measurement of extinction and backscatter profiles in cirrus clouds by using a combined Raman elastic–backscatter lidar, *Appl. Opt.*, *31*, 7113–7131, 1992.

Auer, A. H., Jr., and D. L. Veal, The dimension of ice crystals in natural clouds, *J. Atmos. Sci.*, *27*, 919–926, 1970.

Baumgardner, D., J. E. Dye, B. W. Gandrud, and R. G. Knollenberg, Interpretation of measurements made by the forward scattering spectrometer probe (FSSP-300) during the Airborne Arctic Stratospheric Expedition, *J. Geophys. Res.*, *97*, 8035–8046, 1992.

Borrmann, S., B. P. Luo, and M. Mishchenko, Application of the T-matrix method to the measurement of aspherical (ellipsoidal) particles with forward scattering optical particle counters, *J. Aerosol Sci.*, *31*, 789–799, 2000a.

Borrmann, S., A. Thomas, V. Rudakov, V. Yushkov, B. Lepuchov, T. Deshler, N. Vinnichenko, V. Khattatov, and L. Stefanutti,

Stratospheric aerosol measurements in the Arctic winter of 1996/1997 with the M-55 Geophysika high-altitude research aircraft, *Tellus, 52B*, 1088–1103, 2000b.

Butchart, N., J. Austin, J. R. Knight, A. A. Scaife, and M. L. Gallani, The response of the stratospheric climate to projected changes in the concentrations of well-mixed greenhouse gases from 1992 to 2051, *J. Climate, 13*, 2142–2159, 2000.

Butler, C. F., E. V. Browell, W. B. Grant, V. G. Brackett, O. B. Toon, J. Burris, T. McGee, M. Schoeberl, and M. J. Mahoney, Polar stratospheric cloud characteristics observed with airborne lidar during the SOLVE campaign, in *Advances in Laser Remote Sensing*, A. Dabas, C. Loth, and J. Pelon, eds., Editions de L'Ecole polytechnique, 91128 Palaiseux Cedex, France, 397–400, 2001.

Carslaw, K. S., B. P. Luo, S. L. Clegg, Th. Peter, P. Brimblecombe, and P. J. Crutzen, Stratospheric aerosol growth and HNO_3 gas phase depletion from coupled HNO_3 and water uptake by liquid particles, *Geophys. Res. Lett.*, *21*, 2479–2482, 1994.

Carslaw, K. S., Th. Peter, J. T. Bacmeister, and S. D. Eckermann, Widespread solid particle formation by mountain waves in the Arctic stratosphere, *J. Geophys. Res.*, *104*, 1827–1836, 1999.

Carslaw, K. S., M. Wirth, A. Tsias, B. P. Luo, A. Dörnbrack, M. Leutbecher, H. Volkert, W. Renger, J. T. Bacmeister, and T. Peter, Particle

microphysics and chemistry in remotely observed mountain polar stratospheric clouds. *J. Geophys. Res.*, *103*, 5785–5796, 1998.

Deshler, T., D. J. Hofmann, B. J. Johnson, and W. R. Rozier, Balloonborne measurements of the Pinatubo aerosol size distribution and volatility at Laramie, Wyoming during the summer of 1991, *Geophys. Res. Lett.*, *19*, 199–202, 1992.

Deshler, T., B. Nardi, A. Adriani, F. Cairo, G. Hansen, F. Fierli, A. Hauchecorne, and L. Pulvirenti, Determining the index of refraction of polar stratospheric clouds above Andoya (69°N) by combining size-resolved concentration and optical scattering measurements, *J. Geophys. Res.*, *105*, 3943–3953, 2000.

Dörnbrack, A., M. Leutbecher, J. Reichardt, A. Behrendt, K.-P. Müller, and G. Baumgarten, Relevance of mountain wave cooling for the formation of polar stratospheric clouds over Scandinavia: Mesoscale dynamics and observations for January 1997. *J. Geophys. Res.*, *106*, 1569–1581, 2001.

Dye, J. E., D. Baumgardner, B. W. Gandrud, S. R. Kawa, K. K. Kelly, M. Loewenstein, G. V. Ferry, K. R. Chan, and B. L. Gary, Particle size distributions in arctic polar stratospheric clouds, growth and freezing of sulfuric acid droplets, and implications for cloud formation, *J. Geophys. Res.*, *97*, 8015–8034, 1992.

Fahey, D. W., K. K. Kelly, G. V. Ferry, L. R. Poole, J. C. Wilson, D. M. Murphy, M. Loewenstein, and K. R. Chan, In situ measurements

of total reactive nitrogen, total water, and aerosol in a polar stratospheric cloud in the Antarctic, *J. Geophys. Res.*, *94*, 11,299–11,315, 1989.

Goodman, J., R. F. Pueschel, E. J. Jensen, S. Verma, G. V. Ferry, S. D. Howard, S. A. Kinne, and D. Baumgardner, Shape and size of contrails ice particles, *Geophys. Res. Lett.*, *25*, 1327–1330, 1998.

Goodman, J., O. B. Toon, R. F. Pueschel, and K. G. Snetsinger, Antarctic stratospheric ice crystals, *J. Geophys. Res.*, *94*, 16,449–16,457, 1989.

Hansen, J. E., and L. D. Travis, Light scattering in planetary atmospheres, *Space Sci. Rev.*, *16*, 527–610, 1974.

Hartmann, D. L., J. M. Wallace, V. Limpasuvan, D. W. J. Thompson, and J. R. Holton, Can ozone depletion and global warming interact to produce rapid climate change?, *P. Natl. Acad. Sci. USA*, *97*, 1412–1417, 2000.

Heymsfield, A., Ice particles observed in a cirriform cloud at −83°C and implications for polar stratospheric clouds, *J. Atmos. Sci.*, *43*, 851–855, 1986.

Heymsfield, A. J., and C. M. R. Platt, A parameterization of the particle size spectrum of ice clouds in terms of the ambient temperature and the ice water content, *J. Atmos. Sci.*, *41*, 846–855, 1984.

Hostetler, C. A., P. L. Lucker, M. T. Osborn, J. Burris, and T. McGee,

Observations of PSCs and stratospheric aerosols from the LaRC Aerosol lidar, in *Abstracts*, Solve · Theseo 2000 Science Meeting, Palermo, Italy, 127, 2000.

Jäger, H., and D. Hofmann, Midlatitude lidar backscatter to mass, area, and extinction conversion model based on *in situ* aerosol measurements from 1980 to 1987, *Appl. Opt.*, *30*, 127–138, 1991.

Kawa, S. R., D. W. Fahey, K. K. Kelly, J. E. Dye, D. Baumgardner, B. W. Gandrud, M. Loewenstein, G. V. Ferry, and K. R. Chan, The Arctic polar stratospheric cloud aerosol: Aircraft measurements of reactive nitrogen, total water, and particles, *J. Geophys. Res.*, *97*, 7925–7938, 1992.

Kirk-Davidoff, D. B., E. J. Hintsa, J. G. Anderson, and D. W. Keith, The effect of climate change on ozone depletion through changes in stratospheric water vapour, *Nature*, *402*, 399–401, 1999.

Koop, T., K. S. Carslaw, and Th. Peter, Thermodynamic stability and phase transitions of PSC particles, *Geophys. Res. Lett.*, *24*, 2199–2202, 1997.

Luo, B., U. K. Krieger, and T. Peter, Densities and refractive indices of $H_2SO_4/HNO_3/H_2O$ solutions to stratospheric temperatures, *Geophys. Res. Lett.*, *23*, 3707–3710, 1996.

Marti, J., and K. Mauersberger, Laboratory simulations of PSC particle formation, *Geophys. Res. Lett.*, *20*, 359–362, 1993

McGee, T. J., J. F. Burris, W. Hoegy, W. Heaps, D. Silbert, L. Twigg, G. Sumnicht, R. Neuber, T. Schmidt, C. Hostetler, G. M. Hansen, P. L. Lucker, W. H. Hunt, R. M. Lawrence, and M. T. Osborn, AROTEL – an airborne ozone, aerosol and temperature lidar, in *Abstracts*, Solve · Theseo 2000 Science Meeting, Palermo, Italy, 71, 2000.

Mehrtens, H., U. von Zahn, F. Fierli, B. Nardi, and T. Deshler, Type I PSC-particle properties: Measurements at ALOMAR 1995 to 1997, *Geophys. Res. Lett.*, *26*, 603–606, 1999.

Middlebrook, A. M., B. S. Berland, S. M. George, M. A. Tolbert, and O. B. Toon, Real refractive indices of infrared-characterized nitric acid/ice films: Implications for optical measurements of polar stratospheric clouds, *J. Geophys. Res.*, *99*, 25,655–25,666, 1994.

Mishchenko, M. I., Light scattering by randomly oriented axially symmetric particles, *J. Opt. Soc. Am. A*, *8*, 871–882, 1991.

Pueschel, R. F., G. V. Ferry, K. G. Snetsinger, J. Goodman, J. E. Dye, D. Baumgardner, and B. W. Gandrud, A case of type I polar stratospheric cloud formation by heterogeneous nucleation, *J. Geophys. Res.*, *97*, 8105–8114, 1992.

Ravishankara, A. R., and D. R. Hanson, Differences in the reactivity of type I polar stratospheric clouds depending on their phase, *J. Geophys. Res.*, *101*, 3885–3890, 1996.

Reichardt, J., A. Tsias, and A. Behrendt, Optical properties of PSC Ia-enhanced at UV and visible wavelengths: model and observations, *Geophys. Res. Lett.*, *27*, 201–204, 2000.

Shindell, D. T., D. Rind, and P. Lonergan, Increased polar stratospheric ozone losses and delayed eventual recovery owing to increasing greenhouse-gas concentrations, *Nature*, *392*, 589–592, 1998.

Solve · Theseo 2000 Science Meeting, Abstracts, Palermo, Italy, 2000.

Tabazadeh, A., O. B. Toon, and E. J. Jensen, Formation and implications of ice particle nucleation in the stratosphere, *Geophys. Res. Lett.*, *24*, 2007–2010, 1997.

Tsias, A., M. Wirth, K. S. Carslaw, J. Biele, H. Mehrtens, J. Reichardt, C. Wedekind, V. Weiß, W. Renger, R. Neuber, U. von Zahn, B. Stein, V. Santacesaria, L. Stefanutti, F. Fierli, J. Bacmeister, and T. Peter, Aircraft lidar observations of an enhanced type Ia polar stratospheric cloud during APE–POLECAT, *J. Geophys. Res.*, *104*, 23,961–23,969, 1999.

van de Hulst, H. C., *Light Scattering by Small Particles* (Dover, New York, 1981).

Voigt, C., J. Schreiner, A. Kohlmann, P. Zink, K. Mauersberger, N. Larsen, T. Deshler, C. Kröger, J. Rosen, A. Adriani, F. Cairo, G. Di Donfrancesco, M. Viterbini, J. Ovarlez, H. Ovarlez, C. David, and

A. Dörnbrack, Nitric acid trihydrate (NAT) in polar stratospheric clouds, *Science*, *290*, 1756–1758, 2000.

Wandinger, U., A. Ansmann, J. Reichardt, and T. Deshler, Determination of stratospheric aerosol microphysical properties from independent extinction and backscattering measurements with a Raman lidar, *Appl. Opt.*, *34*, 8315–8329, 1995.

Warren, S. G., Optical constants of ice from the ultraviolet to the microwave, *Appl. Opt.*, *23*, 1206–1225, 1984.

Whitby, K. T., and R. A. Vomela, Response of single particle optical counters to nonideal particles, *Environ. Sci. Technol.*, *1*, 801–814, 1967.

Wirth, M., A. Tsias, A. Dörnbrack, V. Weiß, K. S. Carslaw, M. Leutbecher, W. Renger, H. Volkert, and T. Peter, Model-guided Lagrangian observation and simulation of mountain polar stratospheric clouds, *J. Geophys. Res.*, *104*, 23,971–23,981, 1999.

Yang, P., and K. N. Liou, Finite-difference time domain method for light scattering by small ice crystals in three-dimensional space, *J. Opt. Soc. Am. A*, *13*, 2072–2085, 1996.

Yang, P., and K. N. Liou, An efficient algorithm for truncating spatial domain in modeling light scattering by finite-difference technique, *J. Comput. Phys.*, *140*, 346–369, 1998.

Yang, P., K. N. Liou, M. I. Mishchenko, and B.-C. Gao, Efficient

finite-difference time-domain scheme for light scattering by dielectric particles: application to aerosols. *Appl. Opt.*, *39*, 3727–3737, 2000.

Figure Captions

Figure 1. Parameter set of the retrieval algorithm. The parameter values used for illustration are given in the plots.

Figure 2. Scattering phase functions of NAT particles with same d and a_e but different shapes. The wavelength is 532 nm.

Figure 3. Scattering efficiency Q^{sca}, lidar ratio S, and depolarization ratio Δ of single hexagonal crystals as functions of particle maximum dimension for different aspect ratios. The wavelength is 532 nm. S curves of crystals with $a = 2.5$ have been multiplied by 1/3 to fit into the display range. The geometrical-optics limit of Q^{sca} is shown for comparison (thin dash-dotted line).

Figure 4. Scattering efficiency Q^{sca}, lidar ratio S, and depolarization ratio Δ of single hexagonal NAT crystals as functions of aspect ratio for different maximum dimensions. The wavelength is 532 nm.

Figure 5. Scattering efficiency Q^{sca}, lidar ratio S, and depolarization ratio Δ of single hexagonal NAT crystals as functions of particle maximum dimension for different wavelengths λ. The aspect ratio is 0.5.

Plate 1. Initial microphysical parameters (black symbols) and parameters retrieved with the T-matrix-based algorithm (colored symbols) for parameter sets 1–3 (top), and 4–6 (bottom). The 20 best fit results are shown for each

parameter set. multiples can reduce the number of visible data points to less than 20. For initial parameter $d_{0.5}$ see Tab. 3.

Plate 2. Same as Plate 1 but for parameter sets 7–9 (top), and 10–12 (bottom).

Plate 3. Relative difference δA between retrieved and initial surface density versus relative difference δV between retrieved and initial volume density for parameter sets 1–12. The 20 best fit results are shown for each parameter set. multiples can reduce the number of visible data points to less than 20.

Table 1: Functions X and Y.

Function	Extinction coefficient	Backscatter coefficients		
$X(\lambda)$	α_{par}	β_{par}	$\beta_{\text{par}}^{\perp}$	$\beta_{\text{par}}^{\parallel}$
$Y(\lambda, d)$	1	p^{π}	$\frac{\Delta}{1+\Delta}\, p^{\pi}$	$\frac{1}{1+\Delta}\, p^{\pi}$

Table 2: Maximum Dimensions of Particles Used for the Calculations, and Application Ranges of $Y(d_i)$.

i	d_i (μm)	$d_{\min}(i)$ (μm)	$d_{\max}(i)$ (μm)
1	0.20	0.175	0.225
2	0.25	0.225	0.275
3	0.30	0.275	0.325
4	0.35	0.325	0.375
5	0.40	0.375	0.425
6	0.45	0.425	0.475
7	0.50	0.475	0.550
8	0.60	0.550	0.650
9	0.70	0.650	0.750
10	0.80	0.750	0.850
11	0.90	0.850	0.950
12	1.00	0.950	1.100
13	1.20	1.100	1.300
14	1.40	1.300	1.500
15	1.60	1.500	1.700
16	1.80	1.700	1.900
17	2.00	1.900	2.100

Table 3: Initial FDTD Parameter Sets Used for the Retrieval Intercomparison.

Set	$d_{\max}$ (μm)	c	$d_{0.5}$ (μm)	σ (μm)	m (μm^{-1})
1	1.4	−6	1.0	0.25	0.4
2	1.4	−4	1.0	0.25	0.4
3	1.4	−2	1.0	0.25	0.4
4	1.8	−6	1.0	0.25	0.4
5	1.8	−4	1.0	0.25	0.4
6	1.8	−2	1.0	0.25	0.4
7	1.8	−4	1.0	0.25	−0.4
8	1.8	−4	1.0	0.10	0.4
9	1.8	−4	1.0	0.25	0.0
10	1.8	−4	1.0	1.00	0.4
11	1.8	−2	1.0	1.00	0.4
12	1.8	−4	0.5	0.10	0.4

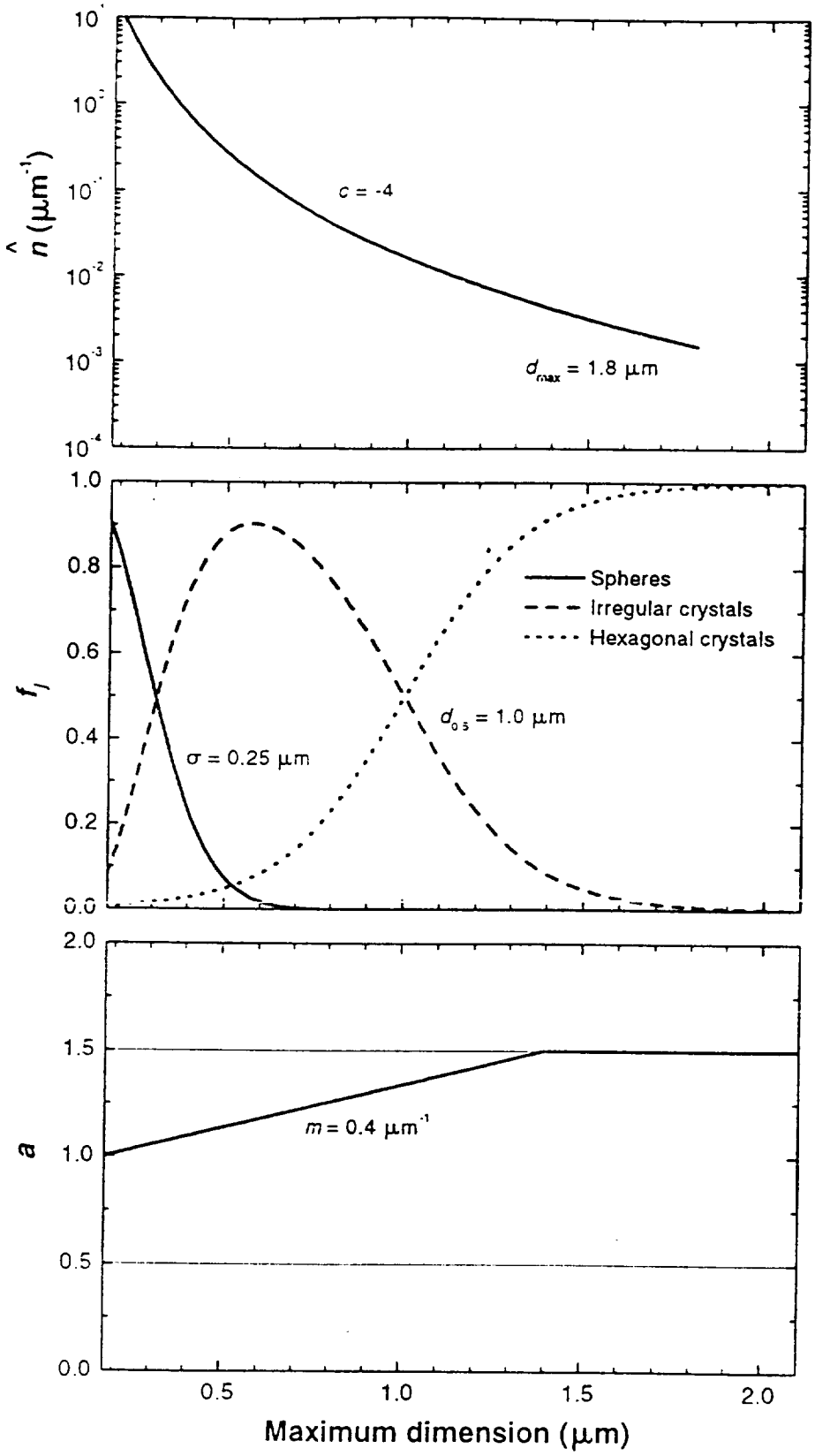

Figure 1. Parameter set of the retrieval algorithm. The parameter values used for illustration are given in the plots.

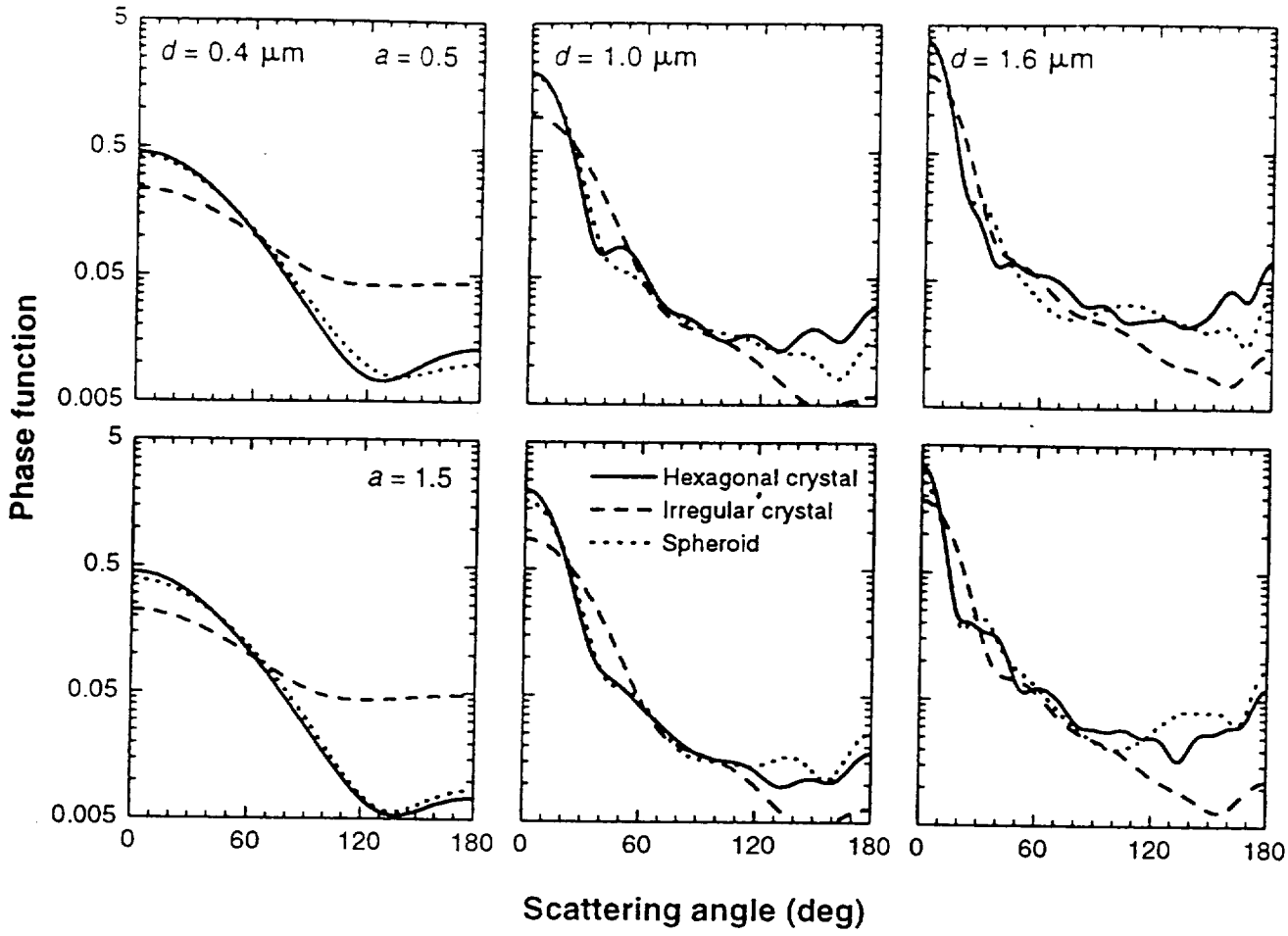

Figure 2. Scattering phase functions of NAT particles with same *d* and *a*, but different shapes. The wavelength is 532 nm.

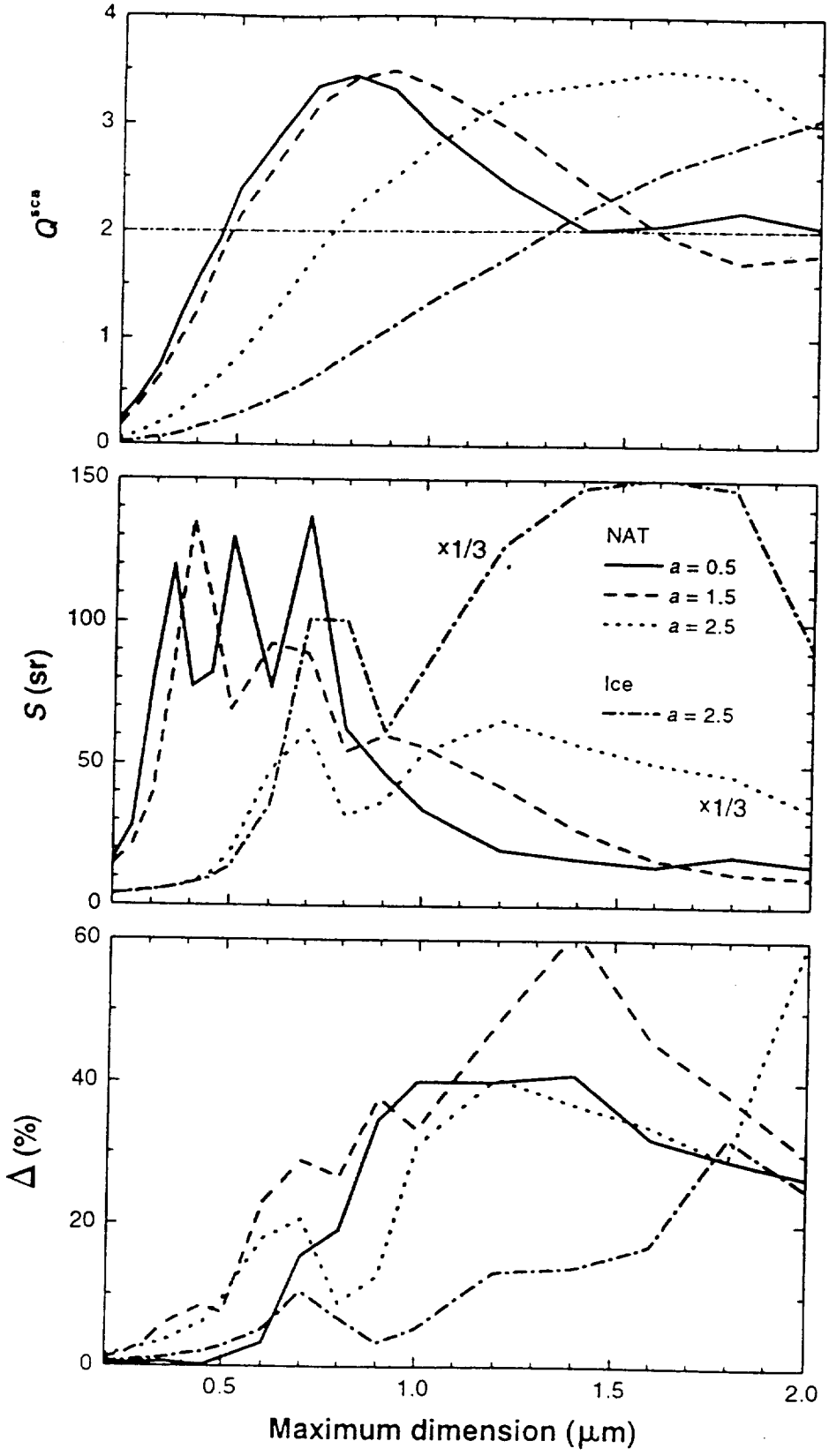

Figure 3. Scattering efficiency Q^{sca}, lidar ratio S, and depolarization ratio Δ of single hexagonal crystals as functions of particle maximum dimension for different aspect ratios. The wavelength is 532 nm. S curves of crystals with $a = 2.5$ have been multiplied by 1/3 to fit into the display range. The geometrical-optics limit of Q^{sca} is shown for comparison (thin dash-dotted line).

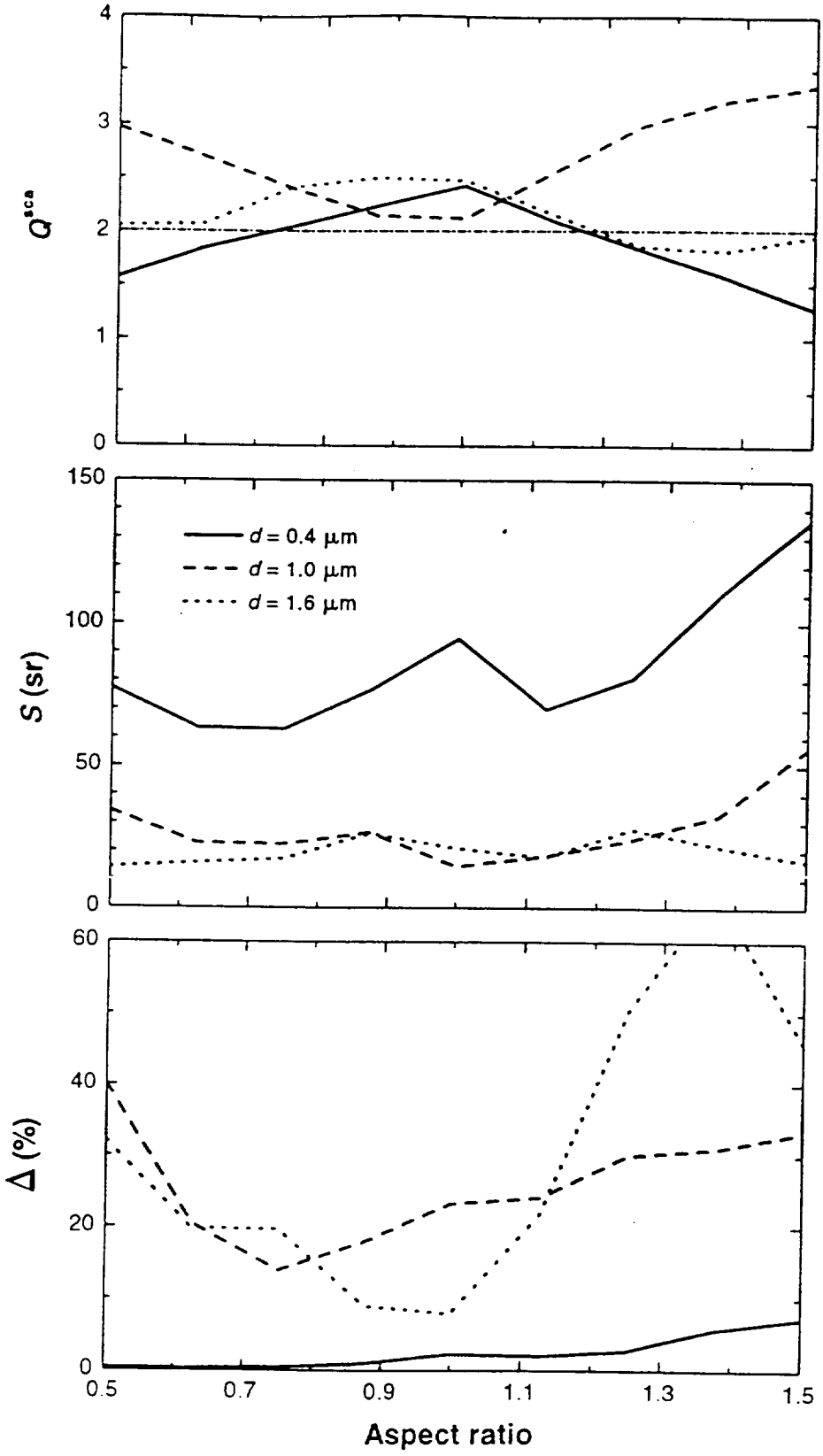

Figure 4. Scattering efficiency Q^{sca}, lidar ratio S, and depolarization ratio Δ of single hexagonal NAT crystals as functions of aspect ratio for different maximum dimensions. The wavelength is 532 nm.

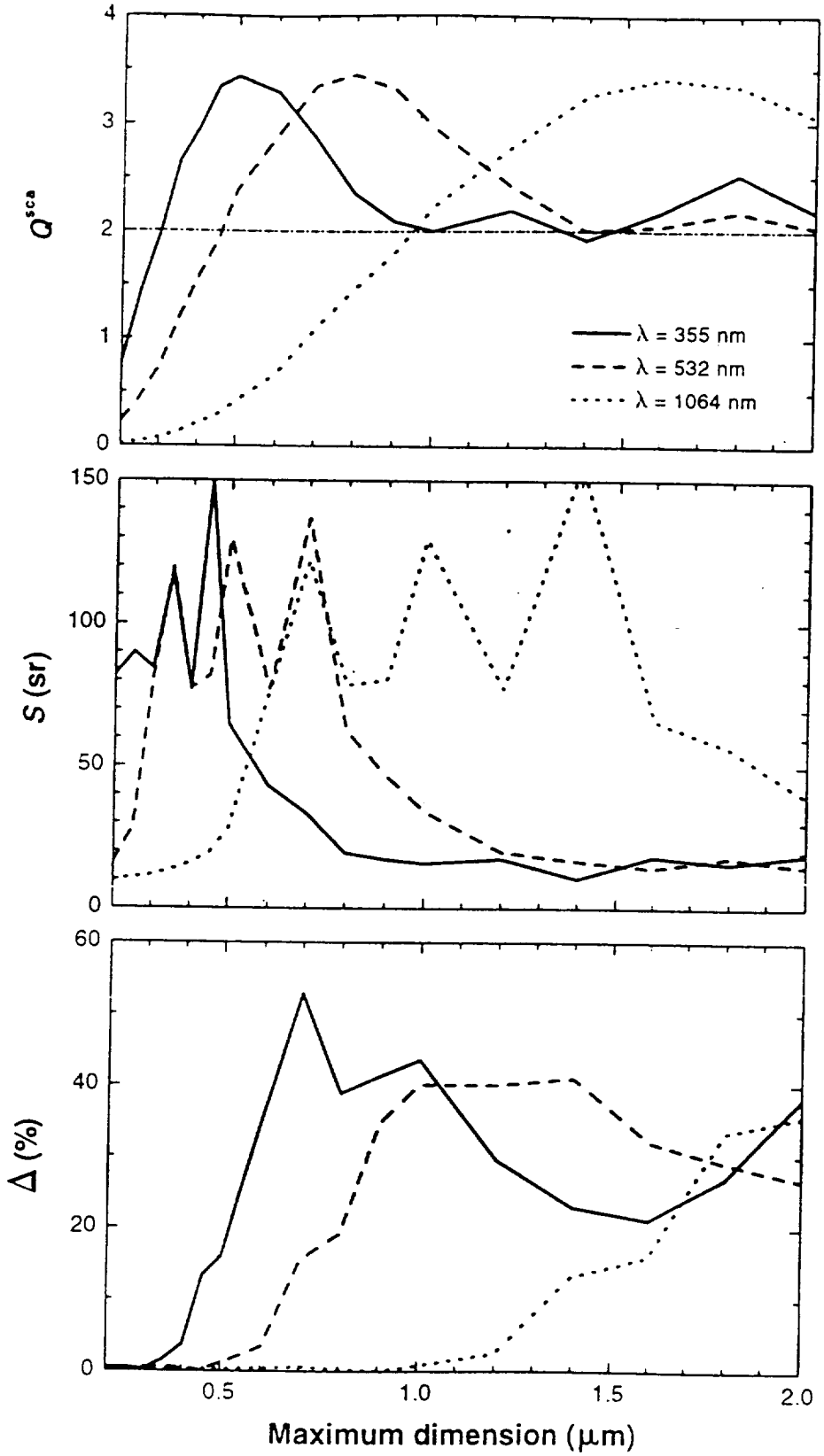

Figure 5. Scattering efficiency Q^{sca}, lidar ratio S, and depolarization ratio Δ of single hexagonal NAT crystals as functions of particle maximum dimension for different wavelengths λ. The aspect ratio is 0.5.

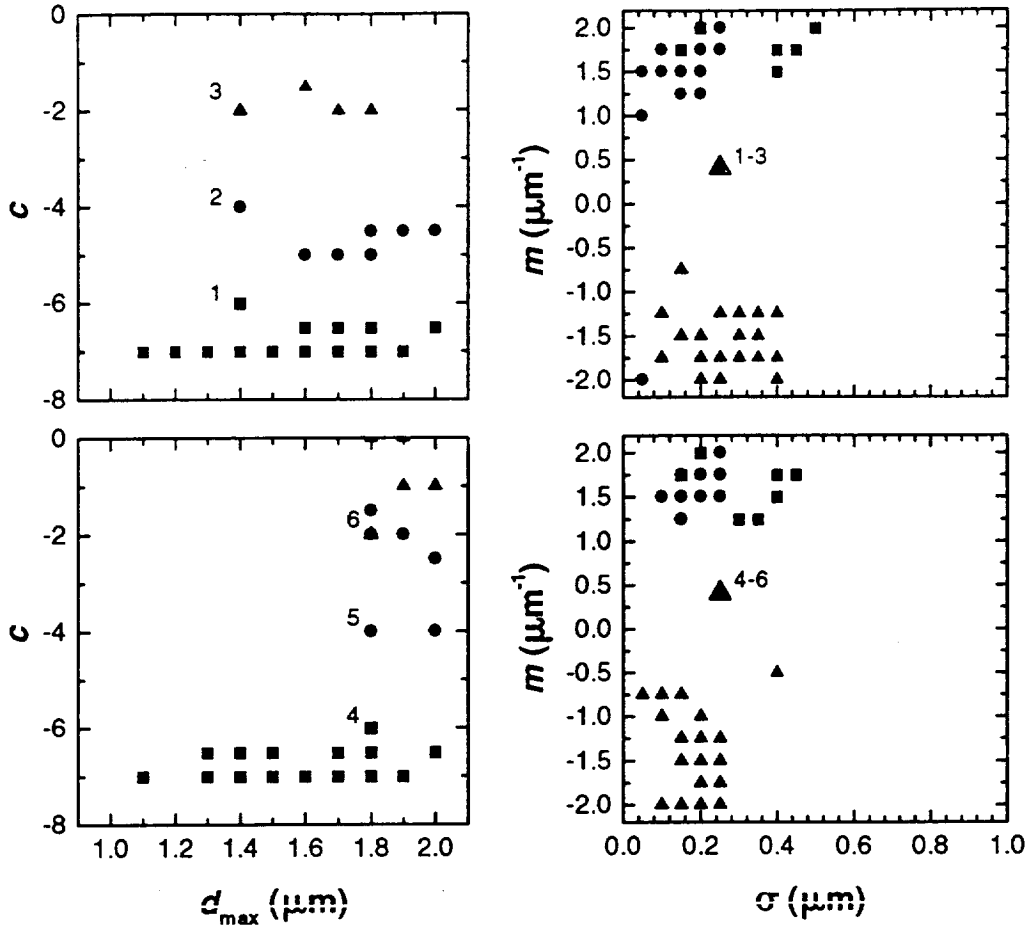

Plate 1. Initial microphysical parameters (black symbols) and parameters retrieved with the T-matrix-based algorithm (colored symbols) for parameter sets 1-3 (top), and 4-6 (bottom). The 20 best fit results are shown for each parameter set, multiples can reduce the number of visible data points to less than 20. For initial parameter $d_{0.5}$ see Tab. 3.

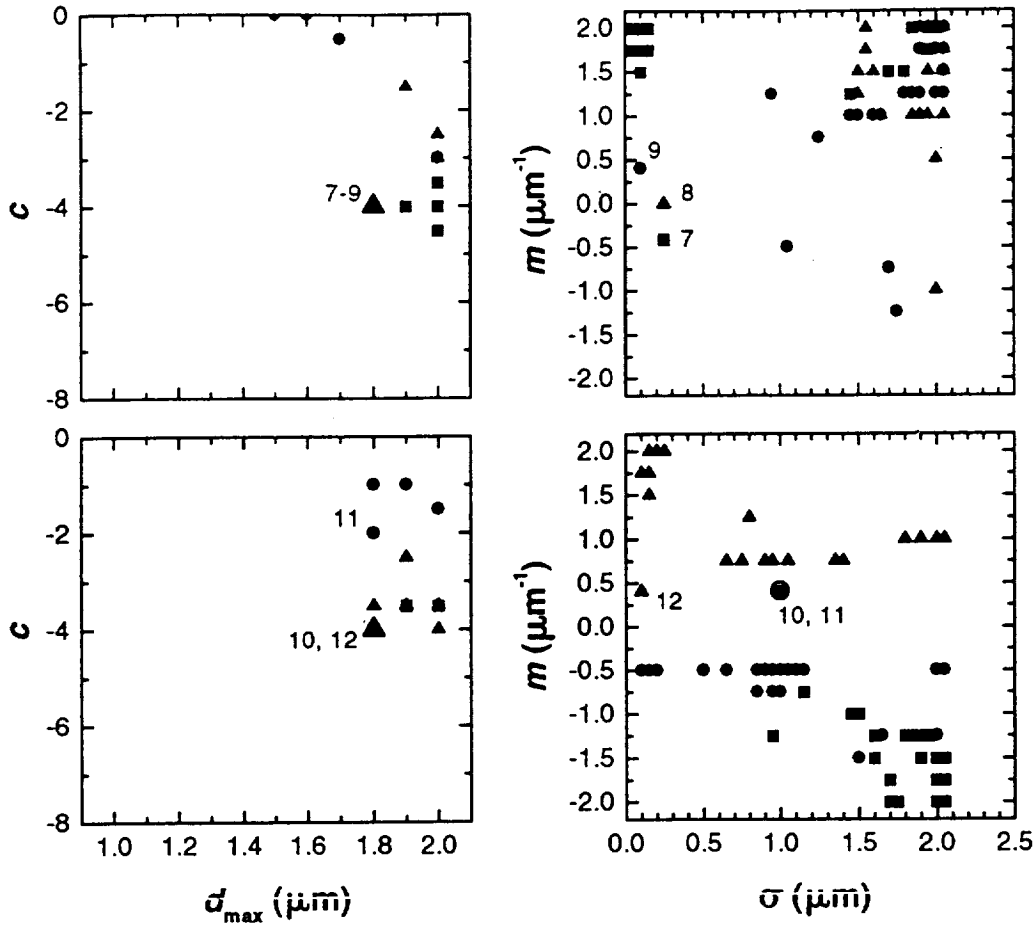

Plate 2. Same as Plate 1 but for parameter sets 7-9 (top), and 10-12 (bottom).

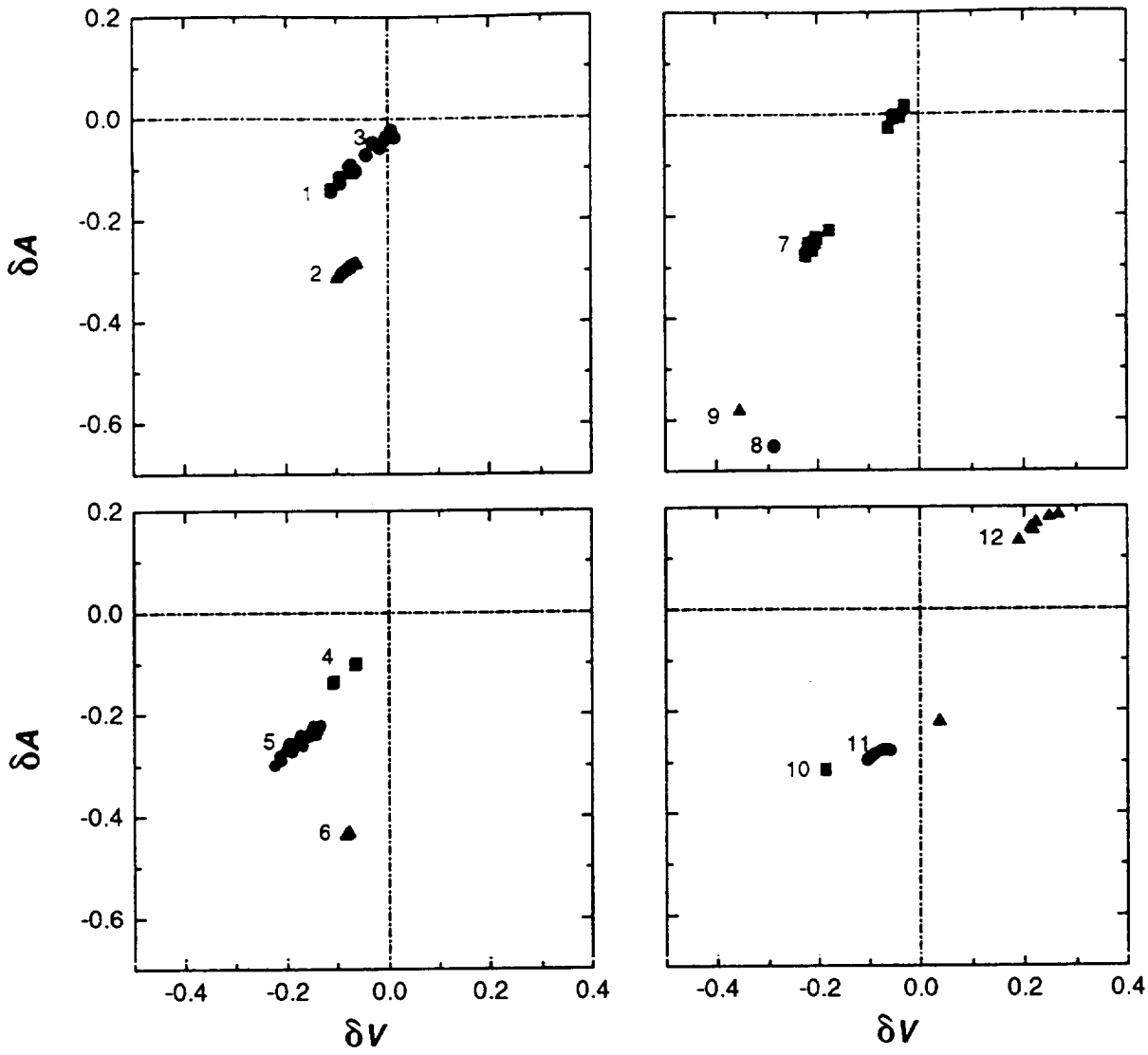

Plate 3. Relative difference δA between retrieved and initial surface density versus relative difference δV between retrieved and initial volume density for parameter sets 1-12. The 20 best fit results are shown for each parameter set, multiples can reduce the number of visible data points to less than 20.